On-chip detection of anisotropic thermopolarization in quartz

Shuichi Iwakiri,* Yasumitsu Miyata, and Takao Mori
National Institute for Materials Science, Tsukuba, Japan

(Received 16 May 2026; accepted 14 September 2026; published 2 November 2026)

Temperature gradients are widely used to drive and probe transport phenomena in solids, forming the basis of heat-to-charge conversion processes. In typical experiments, local heating is introduced to generate a temperature gradient, and the resulting electrical response is detected by separate electrodes. Such measurements usually regard heating purely as a source of thermal excitation. Here, we show that heating inherently generates mechanical stress through thermal expansion, which in turn produces measurable electrical signals via electromechanical coupling. Using quartz as a model piezoelectric system, we demonstrate that heat can be converted to electrical currents via thermally generated stress. The on-chip device used in our experiment enables us to probe the anisotropy of the piezoelectric tensor through the thermally generated current, exhibiting twofold and threefold responses for X-cut and Z-cut crystals, respectively. We further show that the response can be detected in both current and voltage modes. These results reveal a thermomechanical pathway for heat-to-charge conversion and establish a general platform for electrically probing thermomechanical responses in insulating materials.

DOI: 10.1103/2n32-34z8

I. INTRODUCTION

Temperature gradients provide the fundamental driving force for heat-to-charge conversion in solids. In conductors, they generate electrical responses through thermoelectric effects such as the Seebeck effect [1], the Nernst effect [2], and the nonlinear Seebeck effect [3], as well as spin-current generation in the spin Seebeck effect [4]. To probe such phenomena, microfabricated devices consisting of a heater and a detector electrode, hereafter referred to as heater-detector devices, are widely employed. In these devices, a heater generates a temperature gradient via Joule heating [5], while a separate detector electrode detects electrical responses. Within this framework, the heater is typically regarded solely as a source of temperature gradients.

An inevitable consequence of heating, however, is its coupling to mechanics. Thermal expansion, a macroscopic manifestation of phonon anharmonicity, generates strain and stress in solids, which can couple to electrical properties through electromechanical effects such as piezoelectricity [6]. In piezoelectric materials, the polarization $\mathbf{P}$ is linearly related to the stress $\boldsymbol{\sigma}$ through the piezoelectric tensor $\mathbf{d}$ as $\mathbf{P} = \mathbf{d}\,\boldsymbol{\sigma}$, providing a direct mechanism by which thermally generated stress is converted into electrical polarization. In bulk crystals, such coupling is known as secondary pyroelectricity, where thermally induced strain modifies polarization via piezoelectric interactions [7–9].

A representative example is quartz, in which thermally generated stress is converted into polarization through the piezoelectric tensor [7,8,10–12]. Quartz has long served as a model piezoelectric crystal, and the strong orientation dependence of its electromechanical response has been recognized since the earliest studies. In particular, Dawson mapped the angular distribution of piezoelectric surface charges in α-quartz and demonstrated that the piezoelectric response depends strongly on crystal orientation [13]. This implies that thermomechanically generated electrical signals should likewise exhibit a characteristic dependence on crystal orientation, which has also been theoretically suggested [11,12]. While previous studies have primarily relied on bulk measurement setups designed for such effects, this connection suggests that widely used heater-detector devices may also inherently generate and detect thermomechanically induced electrical responses, providing a route to electrically probe insulating materials within a simple device architecture.

In this work, we demonstrate that heater-detector devices can directly detect thermomechanically generated electrical signals, revealing an intrinsic but previously overlooked functionality of this widely used geometry. Using X-cut and Z-cut quartz, we show that the observed signal follows the crystal orientation dependence expected from the piezoelectric tensor. The symmetry is further confirmed by analytical evaluation and finite-element simulations. We also demonstrate that the signal can be detected as both current and voltage across different electrode configurations.

These results establish an on-chip platform for generating thermally induced stress and electrically probing responses in insulating materials. The underlying electromechanical response is not limited to piezoelectricity, but can be extended to more general couplings such as flexoelectricity. In flexoelectricity, the polarization P_i is generated by strain gradients $\partial\varepsilon_{jk}/\partial x_l$, expressed as $P_i = \mu_{ijkl}\partial\varepsilon_{jk}/\partial x_l$ $(i, j, k, l = x, y, z)$ with the flexoelectric tensor μ_{ijkl}. We discuss the

*Contact author: iwakiri.shuichi@nims.go.jp

Published by the American Physical Society under the terms of the Creative Commons Attribution 4.0 International license. Further distribution of this work must maintain attribution to the author(s) and the published article's title, journal citation, and DOI.

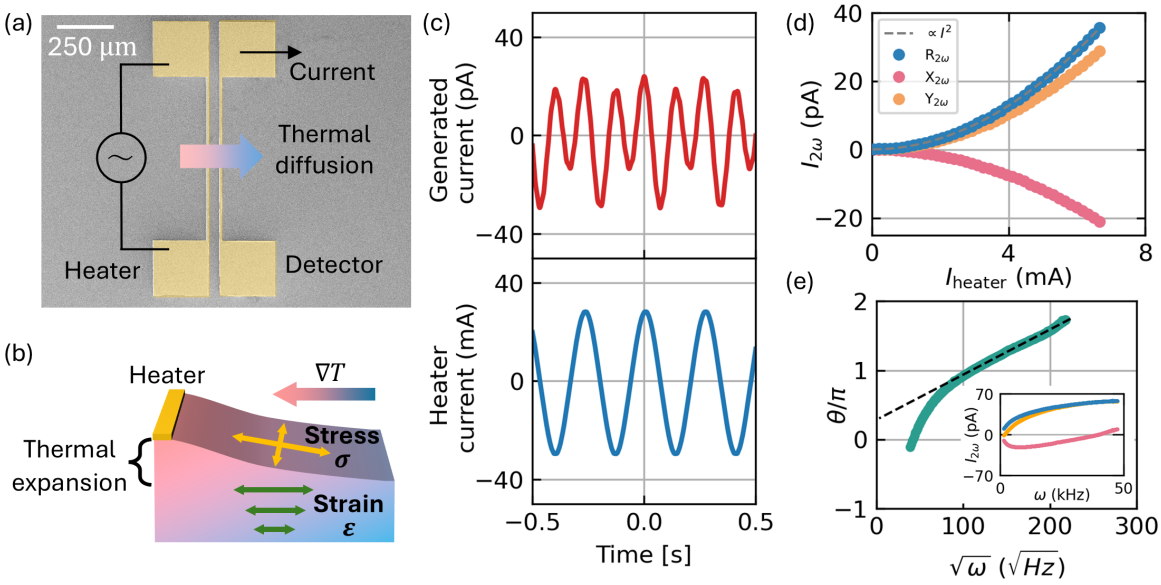


FIG. 1. (a) Image of the device. (b) Schematic of the thermomechanical effects created by an on-chip heater. Thermal stress, strain, and expansion are illustrated. (c) Time-dependent measurement of the generated current measured at the heater (top), compared with the current applied to the heater (bottom). (d) Lock-in detection of the generated current. (e) Lock-in phase of the generated current. The inset shows the frequency dependence of the amplitude.

thermopolarization generated by this mechanism in our accompanying paper [14].

II. DEVICE STRUCTURE

We begin by studying X-cut α-quartz, which possesses a piezoelectric response that converts in-plane stress into out-of-plane polarization [15]. To investigate thermomechanical current generation, we fabricate an on-chip heater and a metallic detection pad onto the quartz substrate, as shown in Fig. 1(a). The heater and the detector patterns are made by maskless photolithography (MicroWriter ML3 Pro, Durham Magneto Optics Ltd.) using AZ-5214E photoresist, baked for 1 min at 100 °C. Both patterns have a width 10 μm and a length 650 μm separated by 40 μm away from each other. Probing pads with 250 μm × 250 μm are attached. After developing the pattern, a 50-nm-thick Au film is formed by rf sputtering, and the resist is carefully lifted off in acetone.

The heater is driven by an alternating current $I = I_{\mathrm{heater}} \sin \omega t$, which produces periodic Joule heating and generates temperature gradients. Under such a thermal gradient, the substrate undergoes space-dependent thermal expansion, which generates lateral stress as illustrated in Fig. 1(b). These thermomechanical fields provide the driving forces for polarization through piezoelectricity in quartz. In the following measurements, an ac excitation voltage $V_0 = 0.004$–2 V at frequency $\omega/2\pi = 0.01$–50 kHz is applied to the heater (resistance $R \simeq 150\ \Omega$). The excitation current is $I_{\mathrm{heater}} = V_0/R$. The detection pad is connected to a transimpedance amplifier (Femto DLPCA-150, FEMTO Messtechnik GmbH), and the resulting current is fed to an oscilloscope or a lock-in amplifier (SRS810, Stanford Research Systems Inc.) with a time constant of 1 s. We detect the second-harmonic voltage at 2ω and convert it to the alternating current $I_{2\omega}$ using the amplifier gain (10^6–10^8 V A^{-1}). For each data point, the lock-in amplifier output voltage was recorded ten times at intervals of 10 s. The mean value and the standard error of the mean were then calculated. The averaged voltage was divided by the transimpedance amplifier gain to obtain the corresponding current.

III. OBSERVATION OF THERMOMECHANICAL CURRENT GENERATION

The thermomechanical-to-electrical conversion yields a current $I \propto \frac{dP}{dt} = \frac{\partial P}{\partial \sigma}\frac{\partial \sigma}{\partial T}\frac{\partial T}{\partial t}$, where P, t, σ, and T denote polarization, time, stress, and temperature, respectively. Here, $\partial P/\partial \sigma$ represents the piezoelectric coupling, $\partial \sigma/\partial T$ corresponds to the thermally induced stress, and dT/dt arises from the time-dependent heating of the device.

Since the heater temperature follows $T(t) \propto I_{\mathrm{heater}}^2 \sin^2(\omega t)$, its time derivative becomes $\frac{dT}{dt} \propto I_{\mathrm{heater}}^2 \sin(2\omega t)$, predicting an electrical response at twice the heater frequency and quadratic in the heater current. Indeed, when the heater is driven at 3 Hz, we observe a clear current signal at 6 Hz, as shown in Fig. 1(c), demonstrating the heat-to-charge conversion. In these measurements, we employ sufficiently low driving frequencies to minimize capacitive coupling between the heater and the detector electrode, which is still visible as the modulation of the detected current amplitude.

To quantify the current generation, we measure the second-harmonic current response $I_{2\omega}$ by lock-in amplifier at 1 kHz. Figure 1(d) shows that both the in-phase (X) and out-of-phase (Y) components of $I_{2\omega}$ increase quadratically with I_{heater}, in agreement with the above observation. We also find that the lock-in phase and its frequency dependence encode the thermal origin of the generated signal. In the device, the temperature approximately follows the one-dimensional diffusion equation $\frac{\partial T}{\partial t} = D\frac{\partial^2 T}{\partial x^2}$, where D is the thermal diffusivity. The solution of the diffusion equation with a sinusoidal heating at

$x = 0$ has the following form:

$$T(x,t) = T_0 e^{-kx} e^{i(\omega t - kx - \frac{\pi}{4})}. \quad (1)$$

Here, the phase lag $k = \sqrt{\frac{\omega}{2D}}$ is the hallmark of the diffusive transport [16–19]. It is important to note that the phase is determined solely by the thermal diffusivity D and experimentally defined parameters. The generated current $I_{2\omega} \propto dT/dt$ inherits the same frequency dependence of the phase.

As shown in Fig. 1(e), we find the phase $\theta(\omega)$ becomes proportional to $\sqrt{\omega}$ at high frequency. From the fitting, we find that the thermal diffusion coefficient of the X-cut quartz to be $\sim(7 \pm 1) \times 10^{-6}\ \mathrm{m^2\,s^{-1}}$, which agrees well with the literature value [20]. The deviation of the data from the fit is due to the breakdown of the one-dimensional thermal diffusion model at low frequency, where the thermal diffusion length is long and heat diffusion into the stage is not negligible [17,18]. This agreement between the experiment and the thermal diffusion model demonstrates that the generated current is of thermal origin.

IV. ORIGIN OF THE GENERATED CURRENT

A. Finite-element method simulation

To gain insight into the origin of the stress and the role of temperature gradient, finite- element method (FEM) calculations are carried out using the coupled temperature-displacement step function of Prepomax v2.4.0 software. This enables the simultaneous simulation of the temperature field and the mechanical displacements.

The simulation employs a rectangular isotropic solid substrate approximating Z-cut quartz with dimensions of 5 mm × 5 mm × 0.5 mm. The bottom surface of the substrate is mechanically and thermally fixed in order to emulate a rigid supporting stage at 20 °C, while no other mechanical constraints are introduced. In the simulations, neither the heater nor the detector electrodes are included explicitly. Instead, the region corresponding to the location of the heater is represented as a localized thermal input volume. The material parameters used in the analysis are as follows. For simplicity, we neglect the anisotropy of physical parameters of quartz. The linear thermal expansion coefficient is $\alpha = 1.33 \times 10^{-5}\ \mathrm{K^{-1}}$, the thermal conductivity is $\kappa = 14.8\ \mathrm{W\,m^{-1}\,K^{-1}}$, and the specific heat capacity is $c_p = 787\ \mathrm{J\,kg^{-1}\,K^{-1}}$. The elastic properties are characterized by a Young's modulus of $E = 7.6 \times 10^{10}$ Pa and a Poisson's ratio of $\nu = 0.17$. The mass density is $\rho = 2.65 \times 10^3\ \mathrm{kg\,m^{-3}}$. The environmental temperature is set to 20°C. For simplicity, the solution is obtained under the steady-state condition. The total Joule heating is calculated from a typical heater resistance of 150 Ω driven by a current amplitude of 4 mA. The geometric volume of the heater region, 650 μm × 10 μm × 100 nm, is used to estimate the nominal power, which amounts to approximately $3700\ \mathrm{W\,mm^{-3}}$.

The simulations show that the temperature increase is concentrated near the heater position and relaxes gradually with distance, as shown in Figs. 2(a) and 2(b). At the heater location, the substrate temperature increases by less than a kelvin, while it returns close to the ambient value within a few hundred micrometers.

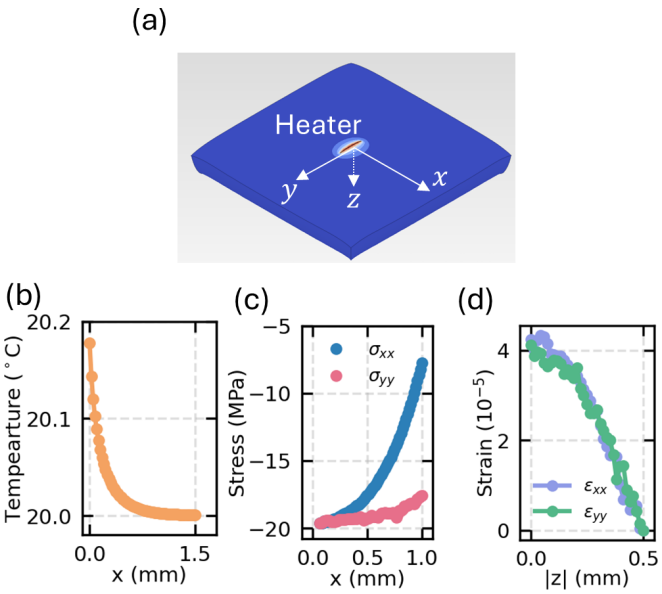


FIG. 2. (a) Schematic of the FEM model used in the calculations. (b) Calculated temperature profile along x axis. (c) In-plane stress along x axis. (d) In-plane strain along the z axis.

Next, the in-plane thermal stresses are analyzed at the same location. The FEM output shows that the stress components σ_{xx} (parallel to the heat flow) and σ_{yy} (perpendicular to the heat flow) are both large near the heater, but relax as the distance from the heater increases [see Fig. 2(c)]. Note that the magnitudes of the strains σ_{xx} and σ_{yy} are similar at $x \sim 0$, while their gradients are significantly different. This relation plays a role in the crystal orientation dependence, as we discuss later.

Finally, the strain distribution normal to the substrate surface is evaluated at the detector located 40 μm away from the heater region. The strain components ε_{xx}, parallel to the in-plane heat-flow direction from the heater, and ε_{yy}, along the long axis of the heater and perpendicular to the heat flow, are computed [see Fig. 2(d)]. Both components exhibit depth-dependent profiles across the substrate thickness, indicating the presence of out-of-plane strain gradients. Such a strain gradient itself does not play a role in piezoelectricity, but contributes to polarization through flexoelectricity in general [14].

These simulations, although simplified, provide consistent evidence that heating leads to the emergence of spatially-dependent strains, in-plane stresses, and out-of-plane strain gradients in the substrate.

B. Phenomenology for the induced charge

Here, we discuss how the polarization generated inside the insulator is converted into the electric current measured at the metallic detector electrode.

First, we consider the easiest phenomenology where the polarization **P** is perpendicular and the electrodes are infinitely large parallel plates [Fig. 3(a)]. Kretschmer and Binder derived a surface charge density ρ induced in such a

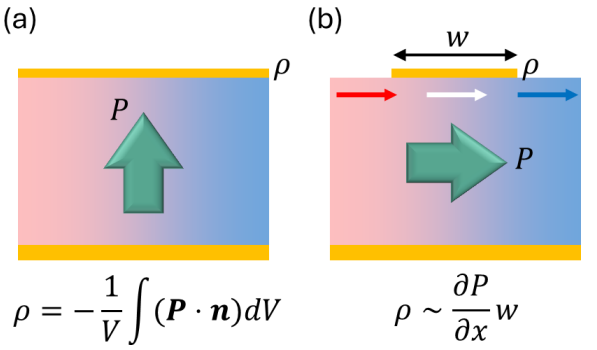


FIG. 3. Models of the surface charge density induced by polarization for (a) a perpendicular polarization with parallel-plate electrodes and (b) an in-plane polarization with a finite-width electrode.

case [21]:

$$\rho = -\frac{1}{V}\int_V \mathbf{P}\cdot\mathbf{n}\, dV. \tag{2}$$

This result is generic for a distributed polarization $\mathbf{P}(\mathbf{r}, t)$. As long as the fringing field is neglected, this formula can be used for electrodes with finite width.

In the present geometry, however, the polarization orients predominantly in-plane [Fig. 3(b)], as we will see in the following section. Also, the electrode has a finite width w and the length is much larger than it. We consider a phenomenology for such a case by approximating the problem as one-dimensional along in-plane axis x. Noting that the polarization can be understood as a pair of positive and negative charges [22], we can assume that only the polarization vectors at the edge of the electrode [red and blue arrows in Fig. 3(b)] contribute to the surface charge, while the one completely beneath the electrode (white arrow) does not contribute to the charge because the image charge created by the negative and positive end of the polarization is canceled. Then, the induced charge is roughly proportional to the difference in polarization across the electrode edges,

$$\rho \propto \frac{\partial P_x}{\partial x} \propto P_x(x+w) - P_x(x), \tag{3}$$

where w is the electrode width. Thus, the electrode effectively detects the spatial variation of the polarization rather than its magnitude. A time-dependent polarization gradient produces a measurable current,

$$I \propto \frac{d\rho}{dt} \propto \frac{\partial^2 P}{\partial t\, \partial x}. \tag{4}$$

V. DECOMPOSING THE STRESS FIELD

The device architecture provides a direct on-chip probe of thermomechanically generated stress. By exploiting the anisotropy of the quartz piezoelectric tensor, the crystal-orientation dependence of the measured current allows the stress components generated by the heater to be identified.

As shown in Fig. 4(a), considering the crystal symmetry of X- and Z-cut quartz, one expects distinct angular responses for different wafer cuts. Z-cut quartz is nearly isotropic in its in-plane thermal conductivity, whereas X-cut quartz

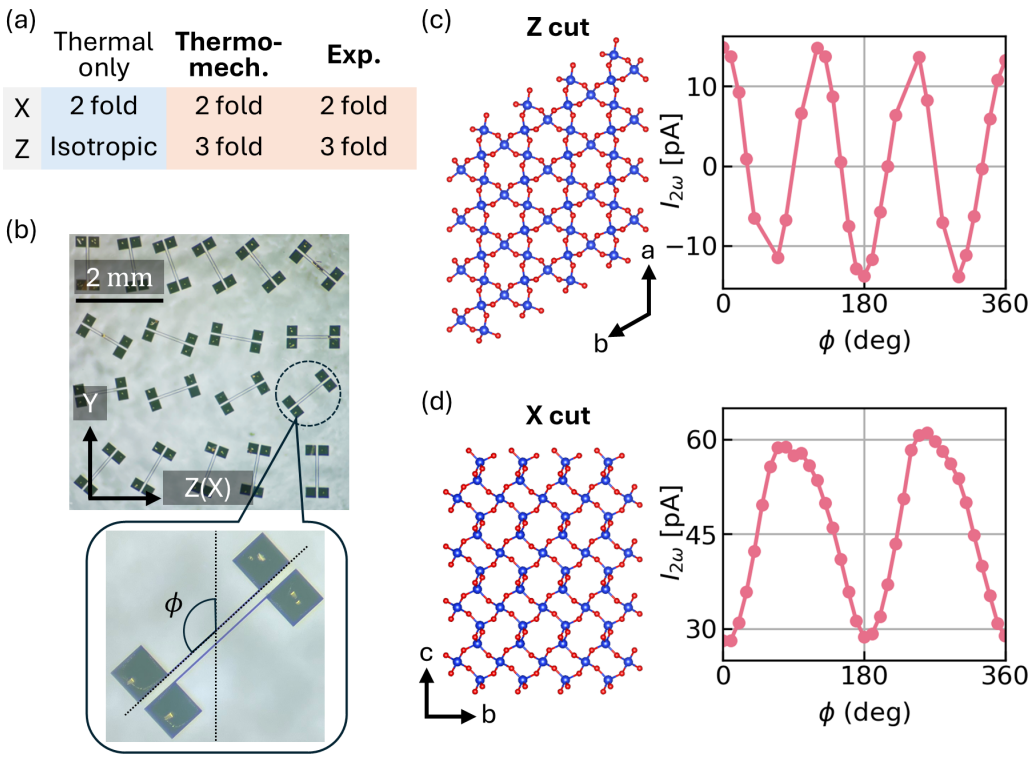


FIG. 4. (a) Expected symmetry in X- and Z-cut quartz for a purely thermal signal, thermomechanical signal, compared with the one observed in our experiment. (b) Picture of the device array used in the angular dependence measurement. (c), (d) Angular dependence of the quadratic component of the generated current in Z-cut and X-cut quartz.

exhibits a twofold anisotropy. Moreover, the piezoelectric tensor produces a threefold symmetry for Z-cut quartz and a twofold symmetry for X-cut quartz. Therefore, the angular dependence of the generated current allows us to distinguish whether the signal originates from thermomechanical coupling or from thermal artifacts.

To probe this behavior, we fabricate an array of devices with the heater-detector axis tilted by an angle ϕ relative to the crystal axes, as shown in Fig. 4(b). The measured responses show the expected symmetry signatures: X-cut quartz exhibits a clear twofold modulation of $I_{2\omega}$ [Fig. 4(c)], whereas Z-cut quartz exhibits a robust threefold modulation [Fig. 4(d)]. These symmetry patterns agree with previous studies on the piezoelectric anisotropy of quartz [11–13]. These observations indicate that the measured current originates from thermomechanically generated stress acting through the piezoelectric tensor.

We next find that the observed angular dependence is the fingerprint of the stress fields in the device. In quartz, the thermal stress couples to the polarization or the displacement field according to the following relation.

The piezoelectric tensor $\mathbf{d}$ of α-quartz [15] is

$$\begin{bmatrix} P_x \\ P_y \\ P_z \end{bmatrix} = \begin{bmatrix} d_{11} & -d_{11} & 0 & d_{14} & 0 & 0 \\ 0 & 0 & 0 & 0 & -d_{14} & -2d_{11} \\ 0 & 0 & 0 & 0 & 0 & 0 \end{bmatrix} \begin{bmatrix} \sigma_{xx} \\ \sigma_{yy} \\ \sigma_{zz} \\ \tau_{yz} \\ \tau_{xz} \\ \tau_{xy} \end{bmatrix}, \tag{5}$$

where P_i is the polarization, σ_{ij} is the stress, and τ_{jk} is the shear with $i, j, k = x, y, z$.

To express the polarization in the device coordinate system fixed on the device plane (x', y', z'), we rotate the piezoelectric relation. Let (x, y, z) denote the crystallographic axes and (x', y', z') the device axes. The two frames are related by an orthogonal rotation matrix R such that $\mathbf{e}_{i'} = R_{i'i}\mathbf{e}_i$. The polarization vector and stress tensor transform as $\mathbf{P}' = \mathbf{R}\,\mathbf{P}$ and $\sigma = \mathbf{R}^{\mathbf{T}}\,\sigma'\,\mathbf{R} = \mathbf{T}\sigma'$. Then, the relation between the polarization and the strain after rotation can be written $\mathbf{P}' = \mathbf{R}\,\mathbf{d}\,\mathbf{T}\,\boldsymbol{\sigma}'$.

In the experiment, the detected signal is primarily sensitive to polarization variations across the short axis of the elongated detector wire (650 μm × 10 μm), where the temperature gradient is the largest. We therefore approximate the detected polarization as $P_{\text{eff}} \simeq P_{x'}, P_{z'}$.

Because the top surface is traction free, the stress components involving the surface normal are expected to be small near the surface. We therefore adopt the plane-stress approximation

$$\sigma_{z'z'} \approx 0, \quad \tau_{x'z'} \approx 0, \quad \tau_{y'z'} \approx 0. \tag{6}$$

A. Z-cut quartz

For Z-cut quartz, the wafer normal coincides with the crystal z axis, and the device rotation corresponds to a rotation about z by angle ϕ:

$$R_z(\phi) = \begin{pmatrix} \cos\phi & -\sin\phi & 0 \\ \sin\phi & \cos\phi & 0 \\ 0 & 0 & 1 \end{pmatrix}. \tag{7}$$

Carrying out the tensor rotation yields

$$P_{x'} = d_{11}(\sigma_{x'x'} - \sigma_{y'y'})\cos 3\phi + 2d_{11}\tau_{x'y'}\sin 3\phi + 2d_{14}\tau_{y'z'}. \tag{8}$$

In this configuration, $P_{z'} = 0$ because the third row of the piezoelectric tensor vanishes. Applying Eq. (6) reduces Eq. (8) to

$$P_{x'} \simeq d_{11}(\sigma_{x'x'} - \sigma_{y'y'})\cos 3\phi + 2d_{11}\tau_{x'y'}\sin 3\phi. \tag{9}$$

Experimentally, the Z-cut signal exhibits an almost pure $\cos 3\phi$ dependence with negligible phase shift and zero offset as shown in Fig. 4(c). The absence of the $\sin 3\phi$ term therefore implies $\tau_{x'y'} \simeq 0$. The polarization thus becomes

$$P_{\text{eff}}(\phi) \simeq d_{11}(\sigma_{x'x'} - \sigma_{y'y'})\cos 3\phi. \tag{10}$$

B. X-cut quartz

For X-cut quartz, the wafer normal coincides with the crystal x axis, and the device rotation corresponds to a rotation about x:

$$R_x(\phi) = \begin{pmatrix} 1 & 0 & 0 \\ 0 & \cos\phi & -\sin\phi \\ 0 & \sin\phi & \cos\phi \end{pmatrix}. \tag{11}$$

The tensor rotation gives

$$\begin{aligned} P_{x'} =& d_{11}\sigma_{x'x'} - d_{11}(\cos^2\phi\,\sigma_{y'y'} + \sin^2\phi\,\sigma_{z'z'}) \\ &+ d_{14}\sin 2\phi(\sigma_{z'z'} - \sigma_{y'y'}) \\ &+ (-d_{11}\sin 2\phi + 2d_{14}\cos 2\phi)\tau_{y'z'}. \end{aligned} \tag{12}$$

The rotation also produces an out-of-plane component

$$\begin{aligned} P_{z'} =& -[d_{11}\sin 2\phi - d_{14}(1 - \cos 2\phi)]\tau_{x'y'} \\ &- [d_{11}(1 - \cos 2\phi) + d_{14}\sin 2\phi]\tau_{x'z'}. \end{aligned} \tag{13}$$

Applying the plane-stress condition simplifies the in-plane polarization to

$$\begin{aligned} P_{x'}(\phi) \simeq& d_{11}\sigma_{x'x'} - \frac{d_{11}}{2}\sigma_{y'y'} - \frac{d_{11}}{2}\sigma_{y'y'}\cos 2\phi \\ &- d_{14}\sigma_{y'y'}\sin 2\phi, \end{aligned} \tag{14}$$

while Eq. (13) reduces to

$$P_{z'} \simeq -[d_{11}\sin 2\phi - d_{14}(1 - \cos 2\phi)]\tau_{x'y'}. \tag{15}$$

Experimentally the response is dominated by the $\cos 2\phi$ term with negligible phase shift as shown in Fig. 4(d). This leads to $\tau_{x'y'} \simeq 0$, making $D_{z'} \simeq 0$, and the leading contribution become

$$P_{\text{eff}}(\phi) \simeq \frac{d_{11}}{2}(2\sigma_{x'x'} - \sigma_{y'y'}) - \frac{d_{11}}{2}\sigma_{y'y'}\cos 2\phi. \tag{16}$$

C. Stress field

According to Eq. (4), the measured current stems from the spatial gradient of the induced polarization, which is generated by the stress. Differentiating the expressions in Eqs. (17) and (18), we obtain current for Z-cut quartz

$$I \propto d_{11} \cos 3\phi \, \frac{\partial}{\partial x}(\sigma_{x'x'} - \sigma_{y'y'}), \tag{17}$$

and for X-cut quartz

$$I \propto \frac{d_{11}}{2} \frac{\partial}{\partial x}(2\sigma_{x'x'} - \sigma_{y'y'}) - \frac{d_{11}}{2} \cos 2\phi \, \frac{\partial \sigma_{y'y'}}{\partial x}. \tag{18}$$

Indeed, Fig. 2(c) shows that the stress gradients satisfy

$$\frac{\partial \sigma_{x'x'}}{\partial x'} > \frac{\partial \sigma_{y'y'}}{\partial x'} > 0, \tag{19}$$

which is consistent with both the observed angular dependences and the signs predicted by Eqs. (17) and (18).

The combined symmetry analysis therefore indicates that the response is dominated by in-plane stresses, whereas shear stresses are negligible. The stress tensor can thus be approximated as

$$\boldsymbol{\sigma}_{\text{surf}} \simeq \begin{pmatrix} \sigma_{x'x'} & 0 & 0 \\ 0 & \sigma_{y'y'} & 0 \\ 0 & 0 & 0 \end{pmatrix}. \tag{20}$$

These results confirm the illustrated stress field in Fig. 1(b), and demonstrates that such a mechanical field-driven response can be captured in our device geometry.

VI. VOLTAGE-MODE DETECTION OF THERMOMECHANICAL POLARIZATION

Finally, to further validate the thermomechanically generated polarization discussed above, we examine its detection in voltage mode.

In the present device geometry, the induced polarization is predominantly oriented in-plane. We therefore first measure the voltage between laterally separated heater and detector electrodes [Fig. 5(a)]. In this setup, the heater is driven by an ac voltage, and we monitor the voltages across both the heater and the detector using a lock-in amplifier operated in second-harmonic mode. The heater is excited with 3 V, which produces a current of approximately 20 mA, at a driving frequency of 100 Hz. For convenience, we measure half of the orientation space from 0° to 180°. As shown in Figs. 5(b) and 5(c), the measured voltage exhibits a clear threefold symmetry for Z-cut quartz, while a twofold symmetry is observed for X-cut quartz. These angular dependencies are consistent with those obtained from current detection (Fig. 4) and directly reflect the symmetry of the in-plane polarization vector.

We further investigate voltage signals measured between electrodes on the top and bottom surfaces of the sample [Fig. 5(d)]. As shown in Figs. 5(e) and 5(f), threefold symmetry is observed for Z-cut quartz and twofold symmetry for X-cut quartz, consistent with the in-plane measurements. In this out-of-plane configuration, the measured voltage is affected by the fringing electric field generated by the predominantly in-plane polarization together with a smaller contribution from the out-of-plane polarization component.

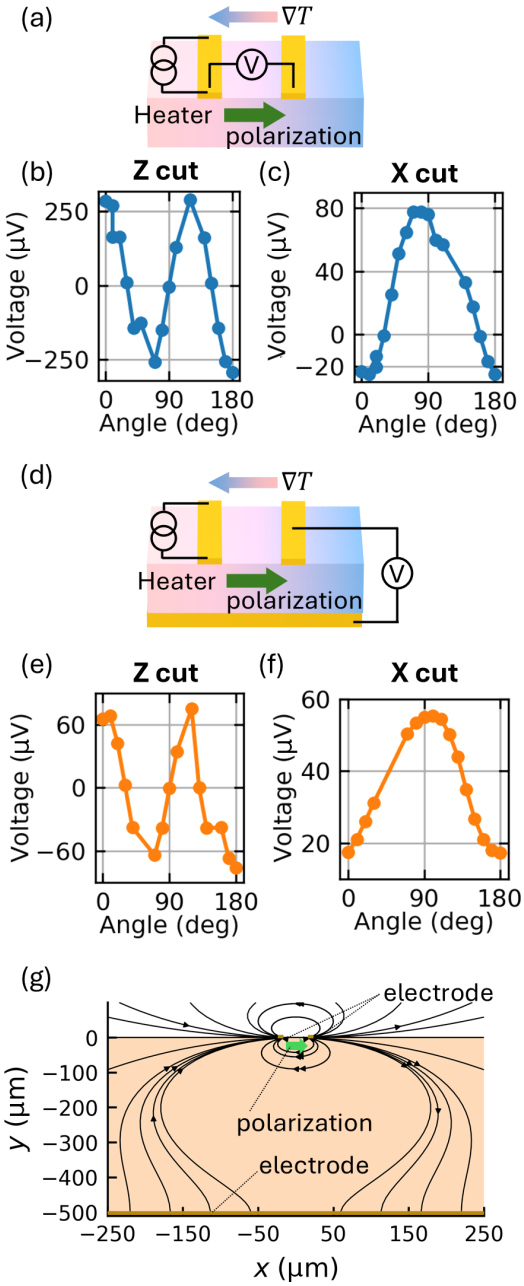


FIG. 5. (a) Schematic of the in-plane voltage detection. Results for (b) Z-cut and (c) X-cut samples. (d) Schematic of the out-of-plane voltage detection. Results for (e) Z-cut and (f) X-cut samples. (g) Cross-section view of the simulated electric field line.

To gain insight into the influence of fringing fields, we perform a two-dimensional electrostatic simulation, as shown in Fig. 5(g). The simulation considers a dielectric containing a uniformly polarized region beneath two electrically floating detector electrodes on the top surface and a continuous bottom electrode, using the same geometry as the experimental device with outer region of the sample grounded. The polarization magnitude is chosen to be $1 \times 10^{-7}\,\mathrm{C\,m^{-2}}$. For simplicity, a uniform dielectric constant of $\varepsilon_r = 4.5$, close to that of quartz, was assumed throughout the simulation domain. The calculated electric-field distribution shows that, unlike the ideal in-plane capacitor geometry where most of

the electric flux is confined between the two detector electrodes, a substantial fraction of the electric flux spreads into the surrounding dielectric and terminates on the bottom electrode through fringing fields. Consequently, only a fraction of the polarization-induced screening charge is collected by the finite top electrodes, while the remaining electric flux is screened by the bottom electrode and the surrounding dielectric. These results indicate that the finite electrode geometry modifies the quantitative relationship between the intrinsic polarization and the measured electrode charge. These results indicate that the finite electrode geometry primarily modifies the quantitative relationship between the intrinsic polarization and the measured electrode charge, while preserving the qualitative angular dependence.

The agreement between current-mode and voltage-mode symmetry provides evidence that the detected signal originates from thermomechanically generated polarization. While voltage-mode detection offers a direct probe of polarization symmetry, quantitative conversion of the measured voltage into polarization depends sensitively on the capacitive coupling and device geometry. In contrast, current-mode detection provides a more direct and quantitative measure of the generated charge. In the Supplemental Material, we provide a more detailed discussion of the origin of the measured signal and estimate the magnitude of thermopolarization. In the accompanying paper, we employ both voltage- and current-mode detection to investigate thermopolarization in generic insulators driven by the flexoelectric effect [14].

VII. DISCUSSION

In this paper, we have focused on the thermopolarization effect in piezoelectric material. As we discuss in the following, the polarization generation due to mechanical stress, namely, the electromechanical coupling, is not restricted to piezoelectricity, but can be generically realized in materials of any symmetry.

In general, electric polarization can be expressed as a nonlocal linear response to the strain field, $P_i(\mathbf{r}) = \int K_{ijk}(\mathbf{r} - \mathbf{r}')\,\varepsilon_{jk}(\mathbf{r}')\,d\mathbf{r}'$, where K_{ijk} is the nonlocal electromechanical response kernel. Taking the Fourier transform gives $P_i(\mathbf{q}) = K_{ijk}(\mathbf{q})\,\varepsilon_{jk}(\mathbf{q})$, where $K_{ijk}(\mathbf{q}) = \int K_{ijk}(\mathbf{s})e^{i\mathbf{q}\cdot\mathbf{s}}d\mathbf{s}$, with $\mathbf{s} = \mathbf{r} - \mathbf{r}'$. For long-wavelength deformations ($|\mathbf{q}\cdot\mathbf{s}| \ll 1$), the exponential function can be expanded as $e^{i\mathbf{q}\cdot\mathbf{s}} = 1 + i\mathbf{q}\cdot\mathbf{s} + O(q^2)$, which yields $K_{ijk}(\mathbf{q}) = K^{(0)}_{ijk} + iK^{(1)}_{ijkl}q_l + O(q^2)$. Transforming this back to the real-space notation, we obtain $P_i = K^{(0)}_{ijk}\varepsilon_{jk} + K^{(1)}_{ijkl}\frac{\partial\varepsilon_{jk}}{\partial x_l}$. The zeroth-order term corresponds to the piezoelectric response in noncentrosymmetric crystals, whereas the first-order strain-gradient term corresponds to the flexoelectric response.

The constraint of these two terms is determined by crystal symmetry. Under spatial inversion, the polarization changes sign, $P(-\boldsymbol{r}) \to -P(\boldsymbol{r})$, whereas the strain remains unchanged, $\varepsilon(-\boldsymbol{r}) \to \varepsilon(\boldsymbol{r})$. Therefore, in centrosymmetric crystals the zeroth-order coefficient must be $K^{(0)}_{ij} = 0$, and the leading contribution becomes $P_i = K^{(1)}_{ijkl}\frac{\partial\varepsilon_{jk}}{\partial x_l}$, which corresponds to the flexoelectric effect. In contrast, in noncentrosymmetric crystals, $K^{(0)}_{ijk}$ is symmetry allowed, leading to $P_i = K^{(0)}_{ijk}\varepsilon_{jk} + K^{(1)}_{ijkl}\frac{\partial\varepsilon_{jk}}{\partial x_l}$.

Consequently, piezoelectric and flexoelectric responses should not be regarded as fundamentally different mechanisms but rather as the zeroth- and first-order terms, respectively, in the same long-wavelength expansion of a general nonlocal electromechanical response. The material dependence is therefore governed primarily by crystal symmetry. Centrosymmetric materials exhibit only the strain-gradient response (flexoelectricity), whereas noncentrosymmetric materials, including quartz, possess both strain and strain-gradient channels.

In the present experimental scheme, local Joule heating produces a highly nonuniform temperature distribution. The resulting thermal expansion generates both strain and strain gradients. In piezoelectric material such as quartz, the strain couples to the polarization, achieving the heat-to-charge conversion as we have seen in this article. This viewpoint also suggests that such a process can be realized even in nonpiezoelectric material thanks to flexoelectricity. The present work therefore establishes the piezoelectric limit of the unified on-chip thermopolarization platform. The accompanying paper [14] presents the same framework to centrosymmetric materials, demonstrating that the same heater-detector architecture enables universal thermopolarization through flexoelectricity.

VIII. CONCLUSION

In summary, we have shown that an on-chip heater-detector device inherently enables the generation and detection of thermomechanically induced electrical signals. Local Joule heating produces spatially nonuniform thermal expansion, which generates in-plane stress fields that couple to electromechanical responses of the material.

Using quartz as a model piezoelectric system, we have demonstrated that thermally generated stress is converted into electrical current through piezoelectric coupling. The observed angular dependence exhibits twofold and threefold symmetries for X-cut and Z-cut crystals, respectively, in agreement with the symmetry of the piezoelectric tensor. Finite-element simulations quantitatively reproduce both the stress distribution and the resulting electrical response, confirming the thermomechanical origin of the signal. Consistent symmetry observed in both current- and voltage-mode measurements further supports this interpretation.

These results reveal a previously overlooked functionality of heater-detector devices as a platform for electrically probing thermomechanical responses in insulating materials. This approach provides a route to investigating coupled thermomechanoelectric effects in materials where conventional electronic transport measurements are not applicable.

ACKNOWLEDGMENTS

The authors are grateful for the fruitful discussion with Dr. Hikaru Watanabe, Dr. Satoshi Ishii, and Dr. Jun Usami. This work was partially supported by the Japan Society for the Promotion of Science (JSPS) KAKENHI Grant No. 25K21685, Murata Science and Education Foundation Grant No. M25AN110, Kanamori Foundation, and TIA Kakehashi Grant. T.M. thanks the support from JST-Mirai Program Grant No. JPMJMI19A1, Japan.

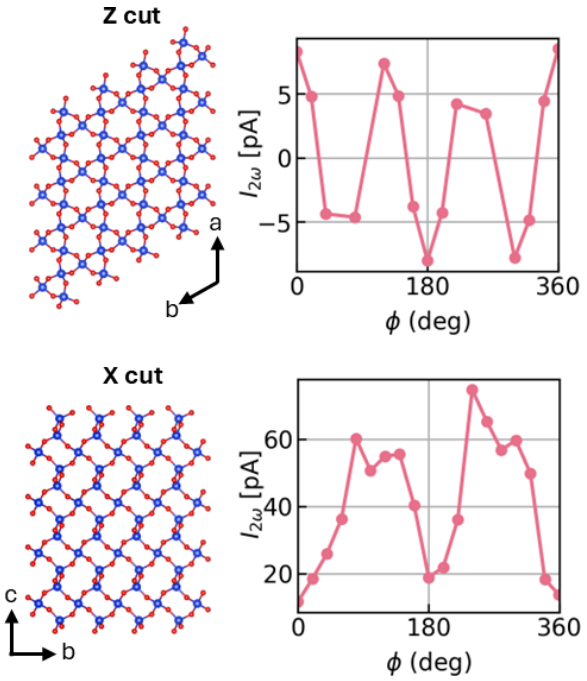


FIG. 6. Angular dependence of the thermopolarization signal measured on additional quartz substrates. The characteristic threefold symmetry is reproduced for Z-cut quartz (top), while the twofold symmetry is reproduced for X-cut quartz (bottom).

DATA AVAILABILITY

There are no publicly available research data or software supporting this manuscript. Requests for further information or data should be sent to the authors.

APPENDIX

1. Reproducibility of the angular dependence

To verify the reproducibility of the observed angular dependence, we perform the same measurements on different quartz substrates obtained by the same supplier from the same crystal batch as those used in the main text.

Devices with the same electrode geometry are fabricated on these substrates, and the second-harmonic current measurements are carried out under the same experimental conditions as those described in the main text. As shown in Fig. 6, the characteristic threefold symmetry for Z-cut quartz and the twofold symmetry for X-cut quartz are consistently reproduced.

Although the absolute signal amplitudes exhibit moderate sample-to-sample variations, the characteristic angular symmetry remains unchanged. Such variations are attributable to small differences in the heater resistance, which modify the Joule heating power and consequently the thermally generated stress. Additional contributions from variations in thermal contact and fabrication tolerances may also be present.

2. Statistical uncertainty of the measured signal

Here, we evaluate the statistical uncertainty of the measured second-harmonic current. For each heater current, the lock-in amplifier output voltage is recorded ten times at intervals of 10 s. The averaged value is used throughout the main text to determine the thermopolarization signal.

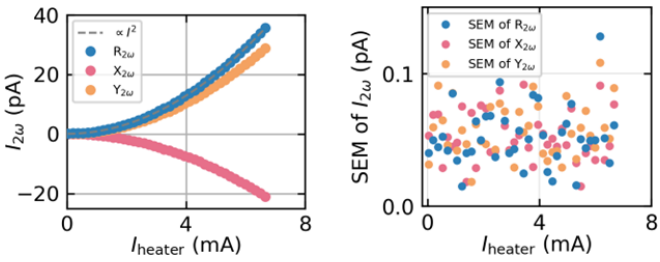


FIG. 7. Measured thermopolarization signal obtained from the averaged lock-in amplifier output (left) and the corresponding SEM estimated from ten repeated measurements (right).

The standard error of the mean (SEM) is calculated from the ten repeated measurements and is used as an estimate of the experimental uncertainty. Figure 7 shows the averaged thermopolarization signal (left) together with the corresponding SEM (right).

The statistical uncertainty is nearly independent of the heater current and is typically less than 1% of the measured signal. Therefore, the experimental uncertainty is significantly smaller than both the measured signal and the symbol size used in the main figures, and does not affect the conclusions of this work.

3. Estimation of the thermopolarization

To evaluate the magnitude of the experimentally observed thermopolarization signal, we compare the current-mode measurement, the voltage-mode measurement, and an order-of-magnitude estimate based on the thermally induced piezoelectric response.

The heater is driven by an ac current at frequency f, producing Joule heating at the second harmonic ($2f$). Consequently, the local temperature, the thermally induced polarization, and the associated screening charge all oscillate at $2f$. Therefore, both the current-mode and voltage-mode measurements originate from the same oscillating screening charge induced at the detection electrode.

a. Converting measured current to charge

In the current-mode measurement, the detection electrode is connected to the input of a transimpedance amplifier (TIA), while the opposite electrode serves as the electrical reference. Since the input node of the TIA is maintained at virtual ground, the oscillating screening charge is directly detected as a nearly short-circuit current.

For an oscillating electrode charge, $Q(t) = Q_{2\omega}\sin(2\omega t)$, the measured current amplitude is $I_{2\omega} = 2\omega Q_{2\omega} = 4\pi f Q_{2\omega}$, where f is the heater excitation frequency. The oscillating charge amplitude is therefore $Q_{2\omega} = \frac{I_{2\omega}}{4\pi f}$.

For the X-cut quartz device at 0°, the measured current is $I_{2\omega} \simeq 1.0 \times 10^{-11}$ A at $f = 1$ kHz, giving $Q_{2\omega} = \frac{1.0\times10^{-11}}{4\pi\times10^{3}} \simeq 8.0 \times 10^{-16}$ C.

Using the active electrode area, $A = 650\ \mu\text{m} \times 10\ \mu\text{m} = 6.5 \times 10^{-9}\ \text{m}^2$, the effective oscillating surface charge density becomes $\frac{Q_{2\omega}}{A} \simeq 1.2 \times 10^{-7}\ \text{C m}^{-2}$.

Because the electric field is highly nonuniform and includes substantial fringing fields, this quantity should be regarded as an effective polarization-equivalent surface charge density collected by the finite detection electrode rather than the intrinsic bulk polarization.

b. Comparison with the piezoelectric response

Next, we compare the experimentally estimated polarization with an order-of-magnitude estimate based on the thermally induced piezoelectric response.

The temperature modulation amplitude at the detector position was calculated by FEM using the experimental geometry and thermal boundary conditions described in the accompanying paper. For a heater current of 4 mA, the temperature modulation amplitude is estimated to be $\Delta T_{\text{FEM}} \simeq 0.4\ \text{K}$.

Using the thermal expansion coefficient of quartz, $\alpha = 1.3 \times 10^{-5}\ \text{K}^{-1}$, the corresponding thermal strain is $\varepsilon_{\text{th}} = \alpha \Delta T_{\text{FEM}} = (1.3 \times 10^{-5})(0.4) \simeq 5.2 \times 10^{-6}$.

Assuming the fully constrained limit, the thermal stress becomes $\sigma_{\text{th}} = E\varepsilon_{\text{th}} = (76.5 \times 10^9)(5.2 \times 10^{-6}) \simeq 4.0 \times 10^5\ \text{Pa} = 0.40\ \text{MPa}$, where $E = 76.5\ \text{GPa}$ is the Young's modulus of quartz.

Using the in-plane piezoelectric coefficient of quartz, $d_{11} = 2.3\ \text{pC N}_{-1}$, the expected polarization is estimated as $P_{\text{piezo}} = d_{11}\sigma_{\text{th}} = (2.3 \times 10^{-12})(4.0 \times 10^5) \simeq 9 \times 10^{-7}\ \text{C m}^{-2}$.

This value is within approximately one order of magnitude of the experimentally obtained effective surface charge density of $Q_{2\omega}/A \simeq 1.2 \times 10^{-7}\ \text{C m}^{-2}$. Considering that the actual device is only partially mechanically constrained and that the finite detection electrode collects only a fraction of the generated polarization charge, this level of agreement is considered reasonable. The result therefore indicates that the experimentally observed signal is consistent, at the order-of-magnitude level, with the thermally induced piezoelectric polarization.

4. Comparison between current- and voltage-mode measurements

The voltage-mode measurement requires additional consideration because the present experiment does not measure the static polarization-induced voltage as shown in Fig. 8. Instead, the sample temperature is periodically modulated, causing the polarization to oscillate at the second harmonic of the heating frequency. Consequently, screening charges continuously flow into and out of the detection electrodes. This oscillating screening current constitutes the common physical origin of both the current-mode and voltage-mode measurements.

Unlike an ideal voltmeter, the differential input of the SR830 lock-in amplifier possesses a finite input impedance of approximately $10\ \text{M}\Omega$ together with finite input and cable capacitances. Therefore, the oscillating screening current develops a voltage across the finite input impedance of the measurement circuit, which is detected by the lock-in amplifier.

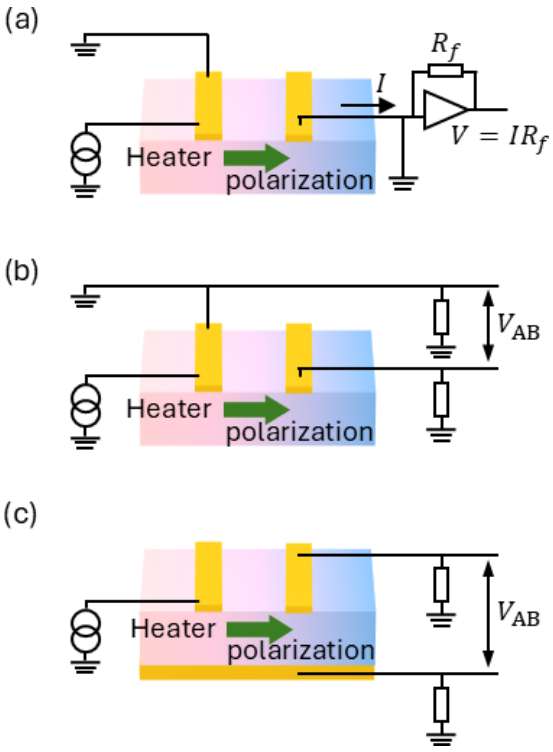


FIG. 8. Schematics of the measurement circuit for (a) current mode, (b) in-plane voltage mode, and (c) out-of-plane voltage mode detection. A transimpedance amplifier with the feedback resistance R_f is shown. White grounded box indicates the input impedance of $10\ \text{M}\Omega$ at the lock-in amplifier.

Experimentally, the measured second-harmonic voltage is on the order of $V_{2\omega} \sim 100\ \mu\text{V}$. This corresponds to a characteristic current of $I_{\text{in}} \sim \frac{100\ \mu\text{V}}{10\ \text{M}\Omega} \sim 10\ \text{pA}$, which is of the same order as the polarization-induced current measured in the current mode.

In conventional electrical measurements, this loading current is negligible because the source current is typically in the nanoampere range or larger. In the present experiment, however, the generated current itself is only of the order of picoamperes. Consequently, the finite input impedance of the lock-in amplifier significantly loads the device, and the voltage-mode measurement is not an ideal open-circuit measurement but rather a loaded one. Accordingly, the current-mode and voltage-mode measurements are naturally expected to yield signals of the same order of magnitude.

Therefore, estimating the polarization directly from the measured voltage using only the geometrical capacitance of the quartz device is not appropriate because such an approach neglects the finite input impedance of the measurement circuit, the input and cable capacitances, and the nonuniform electrostatic coupling associated with the actual electrode geometry.

[1] N. W. Ashcroft and N. D. Mermin, *Solid State Physics* (Saunders College, Philadelphia, PA, 1976).

[2] A. V. Ettingshausen and W. Nernst, Ueber das auftreten electromotorischer kräfte in metallplatten, welche von einem wärmestrome durchflossen werden und sich im magnetischen felde befinden, Ann. Phys. **265**, 343 (1886).

[3] H. Arisawa, Y. Fujimoto, T. Kikkawa, and E. Saitoh, Observation of nonlinear thermoelectric effect in $MoGe/Y_3Fe_5O_12$, Nat. Commun. **15**, 6912 (2024).

[4] K.-I. Uchida, S. Takahashi, K. Harii, J. Ieda, W. Koshibae, K. Ando, S. Maekawa, and E. Saitoh, Observation of the spin Seebeck effect, Nature (London) **455**, 778 (2008).

[5] H. Fangohr, D. S. Chernyshenko, M. Franchin, T. Fischbacher, and G. Meier, Joule heating in nanowires, Phys. Rev. B **84**, 054437 (2011).

[6] W. P. Mason and H. Baerwald, *Piezoelectric Crystals and Their Applications to Ultrasonics* (D. Van Nostrand Company, New York, 1950).

[7] J. Liu and S. T. Pantelides, Mechanisms of pyroelectricity in three- and two-dimensional materials, Phys. Rev. Lett. **120**, 207602 (2018).

[8] R. Masuki, T. Nomoto, R. Arita, and T. Tadano, Full optimization of quasiharmonic free energy with an anharmonic lattice model: Application to thermal expansion and pyroelectricity of wurtzite GaN and ZnO, Phys. Rev. B **107**, 134119 (2023).

[9] J. Liu, M. V. Fernández-Serra, and P. B. Allen, First-principles study of pyroelectricity in GaN and ZnO, Phys. Rev. B **93**, 081205(R) (2016).

[10] A. Jain, D. Mandal, and C. Bera, Pyroelectricity in low-dimensional materials, J. Phys.: Condens. Matter **35**, 415401 (2023).

[11] Yu. M. Poplavko, L. P. Pereverzeva, N.-I. Cho, Y. S. You, and H. G. Nam, Feasibility of microelectronic quartz temperature and pressure sensors, Jpn. J. Appl. Phys. **37**, 4041 (1998).

[12] Yu. M. Poplavko, Piezoelectric intrinsic polarity: Modeling and determination, APL Mater. **13**, 061113 (2025).

[13] L. H. Dawson, Piezoelectricity of crystal quartz, Phys. Rev. **29**, 532 (1927).

[14] S. Iwakiri, Y. Miyata, and T. Mori, Observation of universal thermopolarization effect in insulators, arXiv:2605.17224.

[15] P. Labéguerie, M. Harb, I. Baraille, and M. Rérat, Structural, electronic, elastic, and piezoelectric properties of α-quartz and MXO_4 (M = Al, Ga, Fe; X = P, As) isomorph compounds: A dft study, Phys. Rev. B **81**, 045107 (2010).

[16] A. J. Angström, New method of determining the thermal conductibility of bodies, London, Edinburgh, Dublin Philos. Mag. J. Sci. **25**, 130 (1863).

[17] J. Morikawa and T. Hashimoto, Analysis of high-order harmonics of temperature wave for Fourier transform thermal analysis, Jpn. J. Appl. Phys. **37**, L1484 (1998).

[18] J. Morikawa and T. Hashimoto, Thermal diffusivity of aromatic polyimide thin films by temperature wave analysis, J. Appl. Phys. **105**, 113506 (2009).

[19] J. Ordonez-Miranda, L. Jalabert, Y. Wu, S. Volz, and M. Nomura, Analytical integration of the heater and sensor 3ω signals of anisotropic bulk materials and thin films, J. Appl. Phys. **133**, 205104 (2023).

[20] S. Breuer and F. R. Schilling, Anisotropic thermal transport properties of quartz: From $-120\,^{\circ}$C through the α-β phase transition, Eur. J. Mineral. **33**, 23 (2021).

[21] R. Kretschmer and K. Binder, Surface effects on phase transitions in ferroelectrics and dipolar magnets, Phys. Rev. B **20**, 1065 (1979).

[22] R. Landauer, Electrostatic considerations in $BaTiO_3$ domain formation during polarization reversal, J. Appl. Phys. **28**, 227 (1957).